Uniformity Scan in the Outer Wheel of the Electromagnetic Endcap Calorimeter

P. Barrillon, F. Djama, L. Hinz, P. Pralavorio
CPPM, CNRS/IN2P3 - Univ. Méditerranée, Marseille - France

Abstract

The Module 0 of the electromagnetic endcap calorimeter was assembled and tested with electron beams in 1999. This note shows the results obtained for the uniformity scans in the η and ϕ directions, using the optimal filtering for signal reconstruction both in calibration and physics. Possible sources of non uniformities are reviewed and solutions to reduce their contributions are discussed.

1 Introduction

The module 0 (full-size final prototype) of the liquid argon electromagnetic endcap calorimeter (EMEC) [1] was intensively tested during 3 weeks at CERN, in 1999. It is a highly complex detector since it has to accommodate the accordion geometry in the endcap region. As a result, gap and absorber folding angle vary continuously throughout the detector. To (partially) compensate for the signal change with the gap, high voltage setting also varies by step. The energy variation is thus expected to be of the order of 8% before any correction [2], and the energy resolution may suffer from a higher constant term than in the barrel. The goal of this study is to present the uniformity and resolution of the EMEC after correcting for the effects of high voltage and geometry.

Although not fully equipped in the outer wheel (48 out of 96 electrodes), we were able for the first time to perform these highly detailed studies over a large part of a full-size module. Because of problems encountered during the stacking, the calorimeter was only partially scanned with an electron beam. This analysis is based on 3.6 millions of events (not including the calibration), which correspond to 20% of the total number of events recorded during the test beam period[1].

The study presented here is restricted to the outer wheel ($\eta = [1.375, 2.5]$). The uniformity scans performed in the inner wheel ($\eta = [2.5, 3.2]$) and in the crack between the two wheels ($\eta = 2.5$) are treated elsewhere [3]. First, the main features of the EMEC module 0 are given in section 2. Test beam facilities are then described in section 3. The two different methods of signal reconstruction (optimal filtering and parabola algorithms) are discussed in section 4. The section 5 reviews the results obtained for the uniformity scan analyses. Finally, solutions to improve uniformity are discussed in section 6 and conclusions are drawn in section 7.

2 EMEC module description

Since the outer wheel of the EMEC module is described in details in [1], we will only recall its main features as well as problems encountered during the stacking, which are of primary importance for the results presented in this note.

2.1 Generalities

2.1.1 Granularity

The outer wheel of the detector, projective in pseudo-rapidity (η), is divided in three compartments in depth:

- The front sampling (S1): this sampling is segmented in narrow strips in η, except for the region [1.375,1.5] and [2.4,2.5]. For a given $\Delta\eta = 0.025$ (one S2 cell), the number of strips decreases with η (8, 6 and 4 for [1.5,1.8], [1.8,2.0] and [2.0,2.4], respectively). Same η strips of adjacent electrodes are summed by 12 to construct

[1] There were two test periods: a short one (4 days with a 200 GeV electron beam) and a longer one (two weeks with 10-180 GeV positron beams) where uniformity scans were performed.

	η range				
	[1.375,1.5]	[1.5,1.8]	[1.8,2.0]	[2.0,2.4]	[2.4,2.5]
S1	0.025×0.1 (0-3)×(2-5)	$\sim 0.003 \times 0.1$ (4-99)×(2-5)	$\sim 0.004 \times 0.1$ (100-147)×(2-5)	$\sim 0.006 \times 0.1$ (148-211)×(2-5)	0.025×0.1 (212-215)×(2-5)
S2	0.025×0.025 (0-3)×(8-23)	0.025×0.025 (4-15)×(8-23)	0.025×0.025 (16-23)×(8-23)	0.025×0.025 (24-39)×(8-23)	0.025×0.025 (40-43)×(8-23)
S3	–	0.050×0.025 (0-5)×(8-23)	0.050×0.025 (6-9)×(8-23)	0.050×0.025 (10-17)×(8-23)	0.050×0.025 (18-19)×(8-23)

Table 1: *$\Delta\eta \times \Delta\phi$ of calorimeter cells in the outer wheel. $(\eta_{cell}) \times (\phi_{cell})$ cell numbering ranges are indicated in each region.*

a cell in ϕ ($\Delta\phi = 0.1$). The depth of strips in S1 is 7 and 6 X_0, before and after the step at η= 1.9, respectively.

- The middle sampling (S2): the cell width size in η is constant ($\Delta\eta = 0.025$) and 3 adjacent electrodes with the same η cell are summed in ϕ ($\Delta\phi = 0.025$). Summing S1 and S2 gives a constant length of 24 X_0.
- The back sampling (S3): the η cell size is doubled compared to S2 (same size in ϕ) and the number of X_0 runs from 4 to 14 with increasing η.

The detailed granularity of the detector is summarized in Table 1.

2.1.2 High voltage

The calorimeter response, *i.e.* the peak current (I_{peak}), can be written as [4]:

$$I_{peak} \sim \frac{f_{samp}}{g} \times E_{field}^{0.3} \sim \frac{f_{samp}}{g^{1.3}} \times U^{0.3} \tag{1}$$

where g is the gap between electrodes and absorbers, f_{samp} the sampling fraction and U, the high voltage (HV). Because of the endcap geometry, g decreases with η from roughly 3 to 1 mm. As the absorber's thickness is constant, the sampling fraction follows, to first order, the same variation. Consequently, for a given constant electric field (E_{field}), the dependences of f_{samp} and g with η almost cancel out.

However, in practice, high voltages are set by projective HV sectors (7 in the outer wheel), first approximation to get a constant electric field. The expected calorimeter response from the simulation is shown in Figure 1, as well as the high voltage settings. The peak current per MeV (current density, i_0^E) increases linearly with η inside each HV sector, with a slope h_i^l in the sampling i and HV sector l:

$$I_{peak} = i_0^E \times E_{el} \ , \quad i_0^E = I_0^E \times \left(1 + h_i^l \cdot (\eta - \eta_{center}^l) + O(\eta - \eta_{center}^l)^2\right) \tag{2}$$

where η_{center}^l is the center of the considered high voltage sector, E_{el} the energy of the incident electron and $I_0^E \sim 2.45$ nA/MeV [4]. The current density variation does not depend on the sampling and thus $h_1^l = h_2^l = h_3^l = h^l$.

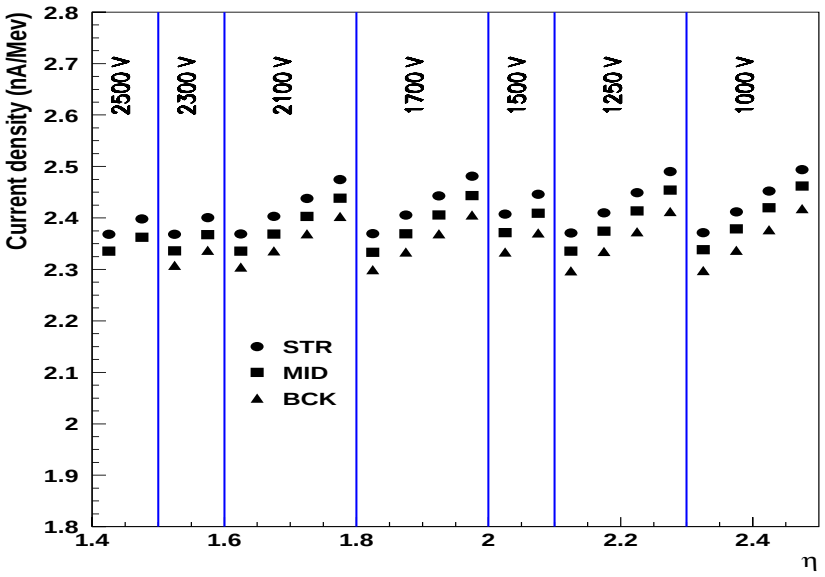

Figure 1: *Simulation of the calorimeter response, current density in nA/MeV, as a function of η [4]. The high voltage values set on the detector are indicated. Vertical lines represent the separation between high voltage sectors.*

2.2 Module 0 stacking and cabling

The outer wheel module assembly consists in stacking absorbers, honeycomb spacer nets and electrodes. Each absorber, with 9 waves accordion shape, is fixed on 8 indexing rings (1 outer, 2 intermediate and 1 inner on front and back side) and the outer radius transversal bar indexed on the structure.

For module 0, a total sagitta of 3 mm was measured on the absorber central wave after the 12 first absorbers (phase I) were mounted. The solution adopted to continue the stacking was to mechanically constraint the absorbers (phase II). This allowed us to stack 48 electrodes, with the drawback of a few induced short circuits between electrodes and absorbers after the complete stacking. No time was left before the test beam to dismount and cure these problems.

2.2.1 Sagging

A typical shape of the sagitta measured for one absorber, in phase I and phase II of the stacking, is plotted in Figure 2a and 2b, respectively. The shape is a parabola with a peak on the 5^{th} wave, in the former case, while it becomes asymmetric in the latter case probably due to non uniform mechanical constraints. The gap value is then systematically greater than the nominal value, especially in S2. Since the absorber is fixed on the indexing rings, S1 and S3 are less affected.

To ease comparison with uniformity scan results, 5^{th} waves' sagitta are now con-

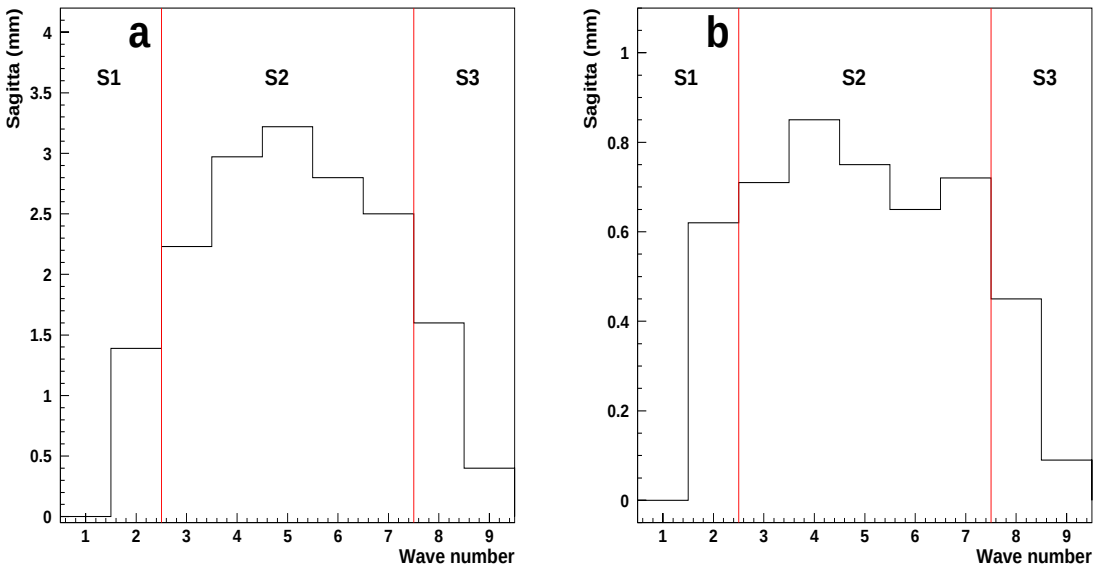

Figure 2: *Typical shape of sagitta as a function of the wave number at* $\eta = 2.2$*, a) in stacking phase I and b) in phase II. Vertical full lines represent the separation between each samplings.*

sidered and averaged over 3 absorbers (size of a S2 cell in ϕ, ϕ_{cell}). Figure 3a shows the sagitta evolution along the stacking, with respect to ϕ_{cell}. Two different slopes are observed: *i*) 1.2 mm per cell for ϕ_{cell} = 8-11 (phase I of the stacking) and *ii*) 0.15 mm per cell for ϕ_{cell} = 12-23 (phase II of the stacking). The sagging amplitude in the latter case is almost constant along 3 ϕ cells (ϕ_{cell} = 12-14) and slightly increases until the end of the stacking.

Figure 3b shows the sagitta value for the 5^{th} wave along η and ϕ_{cell} = 10. Its amplitude increases with η because absorbers are only fixed to the structure at η=1.4.

In conclusion, the sagging problem faced during the stacking implies a gap variation across the detector (in depth, η and ϕ directions) different from predicted. Hence, these problems could be a major source of non uniformity in the detector response.

2.2.2 High voltage problems

During the stacking, high voltage tests were performed on each side of the electrode (HV1 for upper gap, and HV2 for lower gap). If a gap did not hold the nominal value, absorbers and electrode were unstacked and cleaned. This gap was then restacked and tested again till all HV problems were solved. However, at the end of the module stacking, 6% of the channels were found problematic during the complete high voltage test of the module. Unfortunately, no time was left before the test beam to dismount the module and cured these problems. Consequently, the high voltage was not supplied for these channels

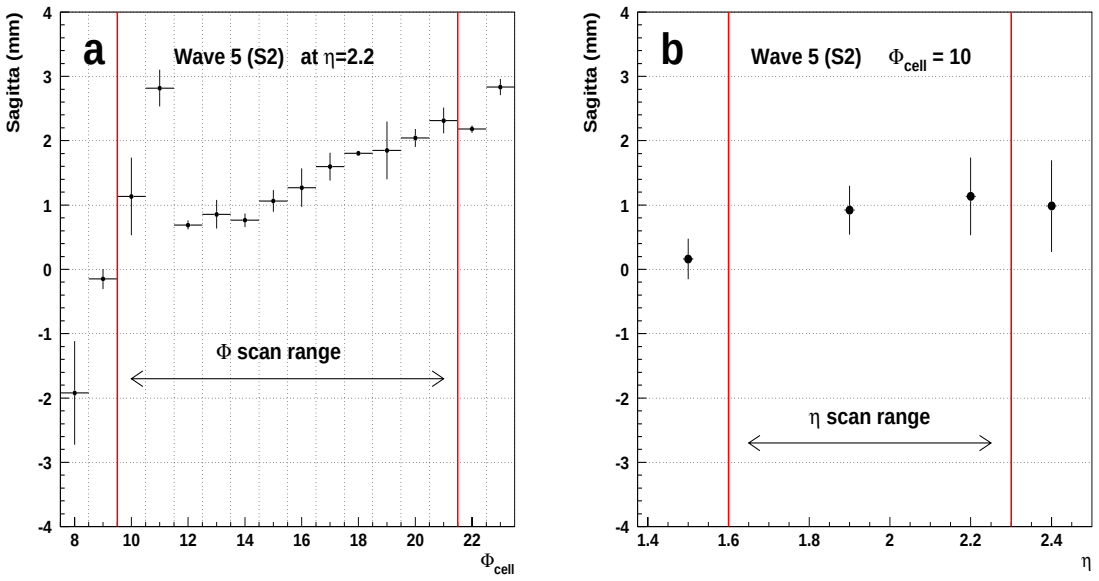

Figure 3: *Sagitta (averaged over 3 absorbers) of the 5^{th} wave: a) as a function of ϕ_{cell} (η=2.2) and b) at 4 η positions ($\phi_{cell} = 10$). The range of ϕ and η scans studied in this note are figured by vertical lines.*

(corresponding pins on HV boards were cut out). Uniformity scan were thus performed on the regions of the detector the least affected by HV problems.

2.2.3 Cold electronics

The module cabling consists in plugging the summing (signal summation in ϕ) and mother boards (calibration and signal routing) on each side of the detector: S1 (S2, S3) channels are connected to the front (back) boards. Detailed crosstalk studies [5] showed that these boards are responsible for most of high inductive crosstalk observed (1-2%) in S2 and S3. The crosstalk amplitude depends mainly on η and identical patterns are observed in each trigger tower (4 cells in S2, *i.e.* $\Delta\eta = 0.1$). This could be a source of non uniformity. The capacitive crosstalk coming from the electrodes is dominant in the strips (2-5%), the front boards contribution being much less pronounced [6].

3 Test beam facilities

3.1 H6 beam

EMEC beam tests took place in the H6 line [7], in the CERN North Area. The beam is produced with SPS protons directed on primary, secondary and eventually tertiary

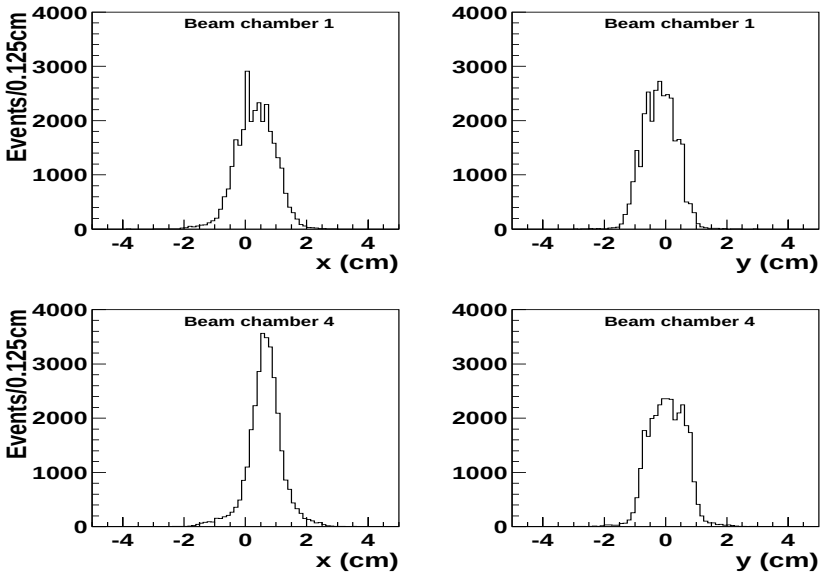

Figure 4: *Beam profile in x and y directions for two chambers located far (upper plots) and near (lower plots) the front side of the detector. x and y coordinates are in the plane orthogonal to the beam direction.*

targets. To perform the uniformity scans, we choose a 100 GeV positron tertiary[2] beam as the best compromise between the event rate, the beam spot size and quality. The collimator settings used are: C3 = $\pm$5 mm, C5 = $\pm$30 mm, C6 = $\pm$30 mm, C8= $\pm$5 mm and gives a momentum spread of $\sigma_p/p = 0.3\%$. This beam (650 events per burst) contains also muons (which are vetoed) and pions (31%) which are flagged and removed in this analysis using the information of scintillator counters located behind the detector. About 3% of randomly distributed non physical triggers are recorded to compute the noise contribution.

Four proportional chambers[8] are in the beam line. Figure 4 shows the beam profile seen by 2 of these chambers. One is situated far the front side of the detector (BC1, $\sim$ 18 m) and the other in its vicinity (BC4, 0.25 m). x and y coordinates are in the plane orthogonal to the beam direction: x is the horizontal direction which corresponds to η and y is the vertical direction which corresponds to ϕ.

The NA31 cryostat is used to test the module in liquid argon. As the beam direction is fixed, the cryostat (detector) is moved to keep the projectivity of the detector in η (ϕ). The cryostat dead material thickness in front of the calorimeter is almost constant with η and amounts to $1 \pm 0.1 X_0$ [9]. In the region $\eta = [1.5 - 1.8]$, the presampler thickness amounts to 0.7 X_0.

[2]A 6 mm lead target is put on the beam line.

3.2 Read out Electronics

ATLAS-like electronics is used to read out the signal. Front End Boards (FEBs), plugged on crates located on the cryostat, amplify and shape the analog signals coming from the mother boards. More precisely, for each input, there are 3 output signals with gain approximately in the ratio 1/10/100 called low/medium/high gain. For the test beam, only high and medium gains are used (the low gain is needed for particles with energy greater than 300 GeV). The output pulses are sampled every 25 ns (40 MHz clock) and then digitized if accepted by the trigger. The digitized signals, in ADC counts, and the time between the trigger and the next leading edge of a 40 MHz clock (time *tdc* in the following)[3] are then recorded.

4 Signal processing

Signal reconstruction consists in finding, after pedestal subtraction, the maximum of each cell response, using n (5 in our case) samples. This section describes two methods to reconstruct the signal, a coarse one – so called parabola – used during the data taking, and a more precise one – named optimal filtering (OF).

4.1 Parabola

Developed for online purpose, this method fits a parabola shape on the 3 highest amplitude samples. This procedure does not rely on any signal shape and can be applied on all detector cells. The systematics introduced by this method can be mainly recover using a reference signal shape. The computed amplitude is thus only affected by a residual bias [10]. The parabola method is however not satisfactory for an ultimate analysis.

4.2 Optimal filtering

The optimal filtering technique, discussed in details in [11], consists of a sum of weighted samples (S_i) to reconstruct the maximum of signal amplitude (A_{max}):

$$A_{max} = \sum_{i=1}^{n} a_i S_i \quad n = 5 \tag{3}$$

A time shift (ΔT, in ns) between reconstructed and input shape maximum amplitude is also computed:

$$A_{max} \cdot \Delta T = \sum_{i=1}^{n} b_i S_i \quad n = 5 \tag{4}$$

a_i and b_i are the optimal filtering weights computed for each gain and for all values of the phase between the trigger and the 40 MHz clock, by step of 1 ns. Two different databases

[3]Since the beam is asynchronous (unlike in ATLAS), the time *tdc* serves as time reference for the digitized samples.

exist for each cell, one for the calibration signal and one for the electron or pion signal (so called 'physics' in this note).

To obtain a_i and b_i from calibration and physics signal shapes, several procedures were tried and are discussed in details in Ref. [12]. In this analysis, we use the following:

- for calibration: a tabulation of the signal shape;
- for physics: a neural network fit [13].

A_{max} is obtained after an iterative process: as input, we choose a set of a_i and b_i coefficients for a given time shift with respect to the 40 MHz clock (0 in calibration, given by time tdc in physics). A_{max} and ΔT are then computed. ΔT is used to determine the new sets of optimal filtering weight coefficients to be used for the next iteration. This procedure is done till the convergence is reached ($|\Delta T| < 1$ ns), usually after 3 iterations. Finally, in physics, A_{max} is computed in high gain if its value is below the saturation and in medium gain in other cases[4].

The optimal filtering will be our standard throughout this note and parabola will only be used for some comparisons.

5 Uniformity scans

The detector was scanned with a 100 GeV positron beam in two directions: *i*) η, one ϕ line ($\phi_{cell} = 10$) and *ii*) ϕ, η lines in the region $\eta \sim 2.2$. A presampler located in front of the calorimeter in the region $\eta = [1.5, 1.8]$ is not used for this study.

5.1 Generalities on data analysis

In uniformity scans, several runs are analyzed with the same procedure: after calibration, high voltage and geometrical effects are parametrized and corrected to obtain the final energy resolution.

5.1.1 Calibration

To get rid of electronics chain variations with time and over all the detector cells, regular calibration runs were taken. Wherever it was possible, we took the closest calibration run preceding the physics run to calibrate the detector[5]. These runs are organized as follows: 11 input calibration pulses with linearly increasing amplitudes[6] are sent, by calibration patterns (4 per sampling), to each input signal line through the mother boards. For each DAC value, A_{max} is reconstructed in ADC counts, after subtraction of the pedestal and

[4] hardware free gain was not available in 1999, and 5 samples were recorded in high and medium gain.

[5] For the region $\eta = 1.6 - 1.7$, we were forced to use a run taken afterwards.

[6] 0-1000 DAC in high gain with a step of 100 DAC, 0-10000 DAC in medium gain with a step of 1000 DAC.

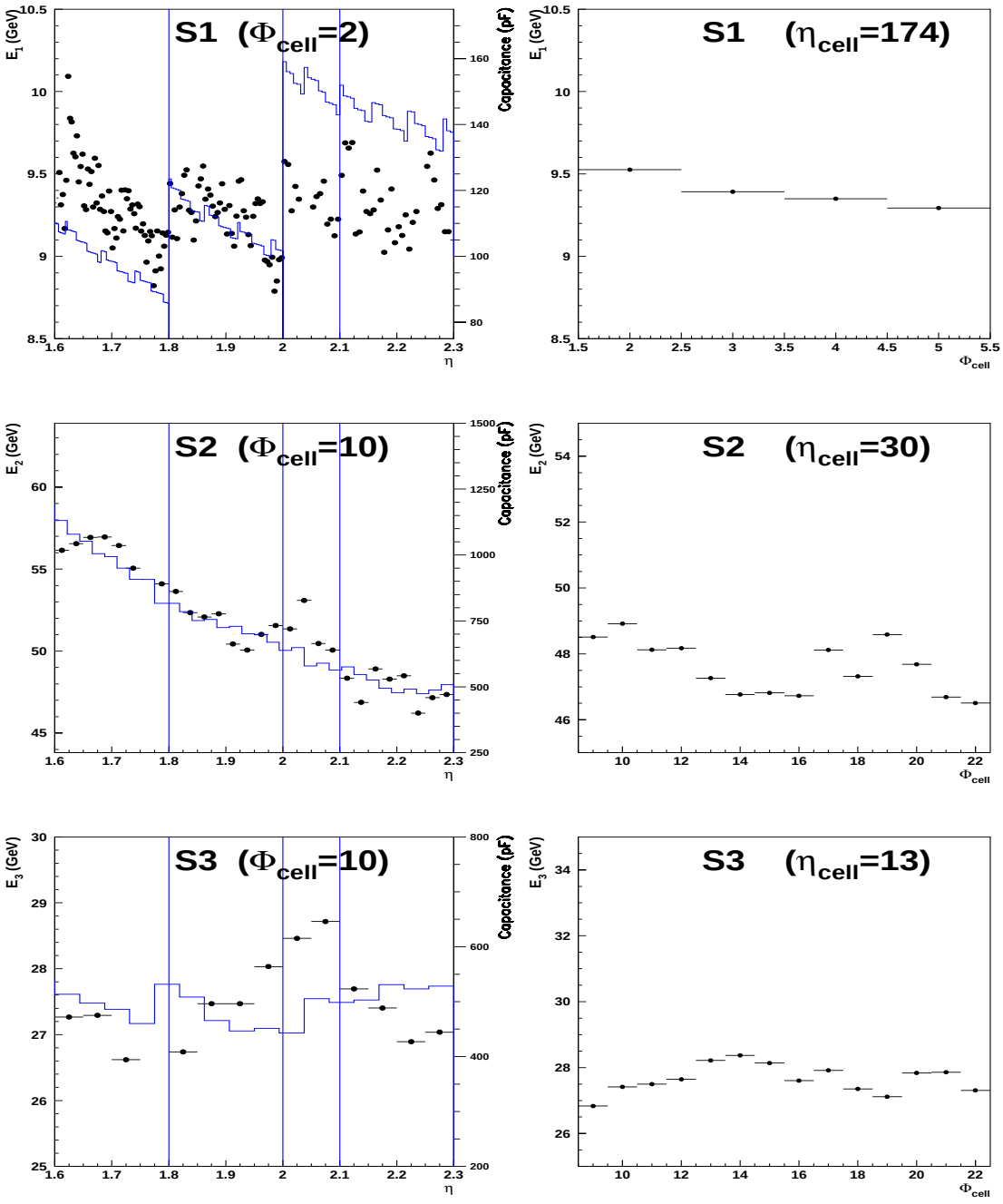

Figure 5: *Cell energy in the 3 samplings versus η (left) and ϕ (right), in the regions scanned by the beam. As input in Equation (5), we use 400 ADC counts in medium gain and reconstruct A_{max} with the optimal filtering method. For left plots, solid histograms represent theoretical cell capacitances (in pF). To ease comparison with Figures presented afterwards, high voltage sectors are shown (vertical lines).*

the calibration board injected charge (DAC=0) [14]. To convert ADC in DAC values, a second degree polynomial

$$DAC = r_1 ADC + r_2 \Big(ADC - r_0 \Big)^2 \tag{5}$$

is fitted with 3 parameters (r_0, r_1 and r_2). r_0, r_1 and r_2 are obtained for each cell in high and medium gains.

The expected factor (γ_i) which converts amplitudes in DAC units to energy in GeV, depends on the sampling, and is given by:

$$E_i = \gamma_i \times DAC \ , \quad \gamma_i = V_{Count}^{DAC} \times \frac{1}{I_0^E} \times \frac{1}{R_i} \tag{6}$$

where V_{Count}^{DAC} is the Volt per DAC conversion factor[7], R_i is the equivalent resistance of the injection system on the mother boards[8], and I_0^E is the current density, cf. Equation (2). Numerically, we obtain:

$$\gamma_2 = \gamma = 31.2 \ MeV \ , \quad \gamma_1 = \frac{\gamma}{6} \ , \quad \gamma_3 = \frac{\gamma}{2} \tag{7}$$

In this analysis, the γ factor computed with the test beam data (cf. section 5.2 and 5.3) is compatible within 10 % with the expected value.

Once calibration coefficients are obtained, it is interesting to look at the variation of the detector response, per sampling, over the calorimeter. As an example, we input 400 ADC counts in medium gain in Equation (5). This value corresponds roughly to A_{max} values obtained for a 100 GeV electron in the S2 cell with maximum energy deposit. Figure 5 shows the cell energy, in each sampling, as a function of η (left) and ϕ (right), in the regions concerned by the beam scan. In the η direction, variation across the detector reflects mainly the cell capacitance changes, as it can be seen when comparing to the theoretical capacitances. As expected, the dependence in ϕ is much less pronounced but still not negligible ($< 4\%$). It may be due to crosstalk and stacking effects.

To estimate the variation of the detector response with time, we calculate the calibration coefficients for 7 runs taken during the test beam period. For an input of 400 ADC counts in medium gain, we compute the energy variation (ΔE) for each channel of the same FEB with respect to a reference run taken at the beginning of the test beam period. Figure 6 shows the normalized energy variation ($\Delta E/E$) distribution, for all channels of one FEB in S2. A good stability of the calibration with time, maximum variation less than 0.5%, is observed.

5.1.2 High voltage correction

To correct for the expected non uniformity coming from the stepped high voltage settings (Figure 1), weights are applied on each cell depending on η, the sampling and the HV sector. The section 5.2.1 shows in detail how these weights are obtained with test beam data. They are then applied before any other steps of the analysis.

[7] The maximum DAC, 5V, is coded on 17 bits, thus $V_{Count}^{DAC} = 5/(2^{17} - 1) = 3.81 \times 10^4$ nV.

[8] $R_i = 3000, 500, 1000\Omega$ for S1, S2 and S3, respectively.

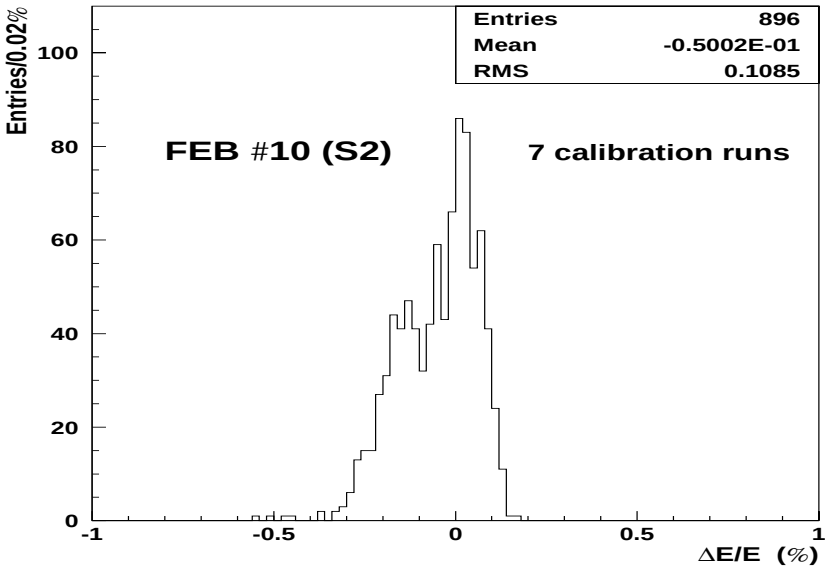

Figure 6: *Normalized energy variation distribution for one FEB in S2 (128 channels). To compute the energy, we use 400 ADC counts in medium gain as input in Equation (5), in each sampling. Results from 7 calibration runs, taken during the test beam period, are shown.*

5.1.3 Clustering

A cluster is constructed, in each sampling, around the cell with maximum energy deposit. Table 2 indicates the cluster sizes considered in this analysis and recall the ones chosen in the ATLAS framework [2].

In S1, we choose an η cluster size of ± 0.03, as suggested by studies performed in the ATLAS frame. Because of changes in the granularity, this corresponds to 23, 15 and 11 strips in the regions [1.5,1.8], [1.8,2.0] and [2.0,2.4], respectively. In ϕ, the cluster contains 1 cell if:

$$|\phi_{S2}^{max} - \phi_{S1}^{center}| < 0.025 \tag{8}$$

or 2 cells if

$$|\phi_{S2}^{max} - \phi_{S1}^{center}| > 0.025 \tag{9}$$

ϕ_{S2}^{max} is the ϕ of the S2 cell with maximum energy deposit, and ϕ_{S1}^{center}, the center of the strip in regard of this cell.

In S2, the cell size decreases continuously with η. We choose a 5×5 cluster (as in TDR) proven to minimize energy leakage at high η. It was not possible to make the same choice in the ϕ scan because of dead cells in the detector, as explained in section 5.3, and we take thus 3×5.

Layer	$\Delta\eta_{cell} \times \Delta\phi_{cell}$ (TDR[2])		
	1.5-1.8	1.8-2.0	2.0-2.4
Strips	$23 \times 1(2)$	$15 \times 1(2)$	$11 \times 1(2)$
Middle	5×5	5×5	5×5
Back	3×5	3×5	3×5

Layer	$\Delta\eta_{cell} \times \Delta\phi_{cell}$ (This analysis)	
	η scan ($\phi_{cell} = 10$)	ϕ scan ($\eta \sim 2.2$)
Strips	TDR	$11 \times 1(2)$
Middle	5×5	3×5
Back	1×1	1×1

Table 2: *Cluster size per layer around cell with maximum energy deposit for TDR analyses (upper table), and uniformity scan analyses (lower table) at 100 GeV.*

In S3, because of the high cross-talk [6] and the low value of the energy deposit, we take the cell in regard of the S2 cell with maximum energy deposit, instead of TDR cluster.

In the following, E_{Si} is the energy measured in the cluster of the sampling i. The total energy (E_{tot}) is defined as the linear sum of E_{Si}. As an example, Figure 7 shows the E_{tot} distribution at $\eta = 1.94$. Energy resolution (σ_E) and mean total energy are extracted from a Gaussian fit performed for $E_{tot} > 98$ GeV[9]. The low tail side of the distribution is non Gaussian because of an electron bremsstrahlung contribution.

Barycenters are computed according to the following formulae:

$$\eta_{bar}^{Si} = \sum_{j=1}^{N_j} \sum_{k=1}^{N_k} \frac{E_i(\eta_j, \phi_k) \times \eta_j}{E_{Si}} \ , \quad \phi_{bar}^{Si} = \sum_{j=1}^{N_j} \sum_{k=1}^{N_k} \frac{E_i(\eta_j, \phi_k) \times \phi_k}{E_{Si}} \tag{10}$$

where $N_j \times N_k$ is the number of cells in a $\Delta\eta \times \Delta\phi$ cluster. Unless otherwise stated, we choose η_{bar}^{S1} and ϕ_{bar}^{S2} as barycenter in η and ϕ, respectively. Extrapolation from beam chambers are not used in this study. As a consequence, barycenter bias (especially 'S-shapes') are not corrected.

5.1.4 Geometrical corrections

Once the total energy is obtained, two geometrical corrections are applied. The η lateral leakage, caused by the finite size of the cluster, and the ϕ-modulation, induced by the accordion geometry. In both case, the corrected energy is computed as:

$$E_{tot}^{corr} = \frac{E_{tot}(s)}{f(s)} \ , \ s \ = \ \eta \ , \phi \tag{11}$$

[9] 98% of the mean energy more generally.

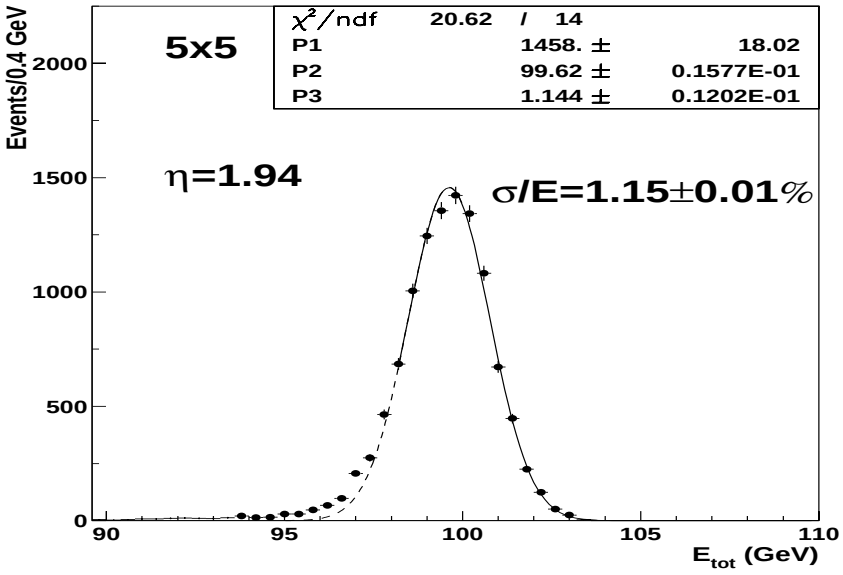

Figure 7: *Total energy distribution at $\eta = 1.94$ ($\phi_{cell} = 10$) for a 5×5 cluster in S2. No corrections are applied. The function over the zone chosen for the fit ($E_{tot} > 98$ GeV) is represented with a full line. The dotted line shows the continuation of this function over the full interval.*

where f is the fitted function which parameterizes the normalized energy variation as a function of s. The section 5.2.2 and 5.2.3 explain in details how η and ϕ corrections are obtained.

5.1.5 Singular channels

For what concerns our uniformity scans, some singular channels were found:

- A dead cell in S1 ($\eta \sim 2.05$, $\phi_{cell} = 2$); events with a S2 barycenter located in this dead η_{cell} are removed.
- A strip ($\eta \sim 2.2$, $\phi_{cell} = 2$) with a broken resistor in a HV side (HV2) on the 9th electrode. For events with a S2 barycenter in ϕ near this region, a correction factor is applied to the strip energy (cf. Appendix 1).
- A S2-S3 short-circuit ($\eta = 1.65$, $\phi_{cell} = 10$). We correct for this default: *i*) in calibration, where we take calibration coefficients from neighbors in ϕ, and, *ii*) in physics, where adequate weights are applied on these two cells (cf. Appendix 1).

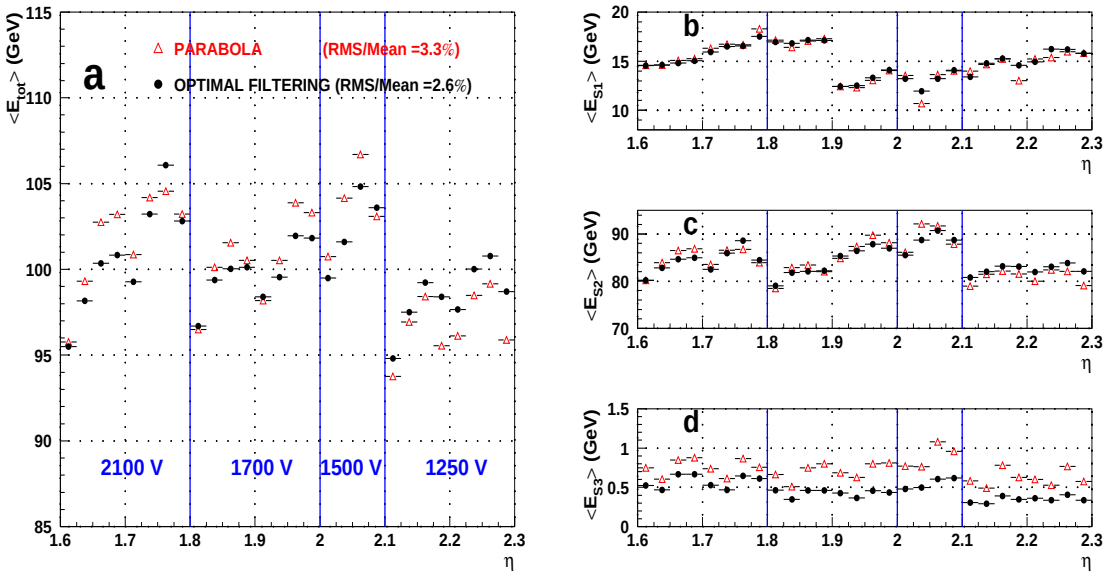

Figure 8: *a) Total and b-d) sampling energies as a function of η cell for the two signal reconstruction methods. Vertical full lines correspond to high voltage sector and vertical dotted lines to separation between summing boards.*

5.2 η scan

An almost complete η scan of the outer wheel ($\eta = [1.6, 2.3]$), centered on $\phi_{cell} = 10$, was performed. The η and ϕ ranges were chosen in the region the least affected by high voltage problems. A total of 28 S2 cells and 4 high voltage regions (out of 7) were scanned.

S2 cell size decreases from 4.9 to 1.5 cm in the η direction. Because of the small beam size in η, cf. Figure 4, we took several runs per S2 cell to obtain a complete coverage of the region $\eta = [1.6, 2.3]$. More precisely, 4, 3 and 2 runs are taken per S2 cell for $\eta \leq 1.7$, $1.7 < \eta \leq 2.0$ and $\eta > 2.0$, respectively[10].

Because of effects coming from the phase I of the stacking, and explained in detail in section 5.3, we consider only events in the center of ϕ cell ($10 \pm 1/6$). None other fiducial cut is applied.

5.2.1 Global view of the η scan

Figure 8a shows the mean value of the total energy as a function of η for optimal filtering and parabola methods. The DAC to GeV conversion factor, γ, is computed to get an averaged total energy of 100 GeV over the scanned zone. At this step, only the calibration is applied. The energy dispersion is 2.6% and 3.3% for the former and later method, respectively. The result of 1.6% estimated from the simulation (Figure 1) can be

[10] A total of 91 runs with 30000 (2×20000) events each were taken for $\eta < 2.0$ ($\eta \geq 2.0$).

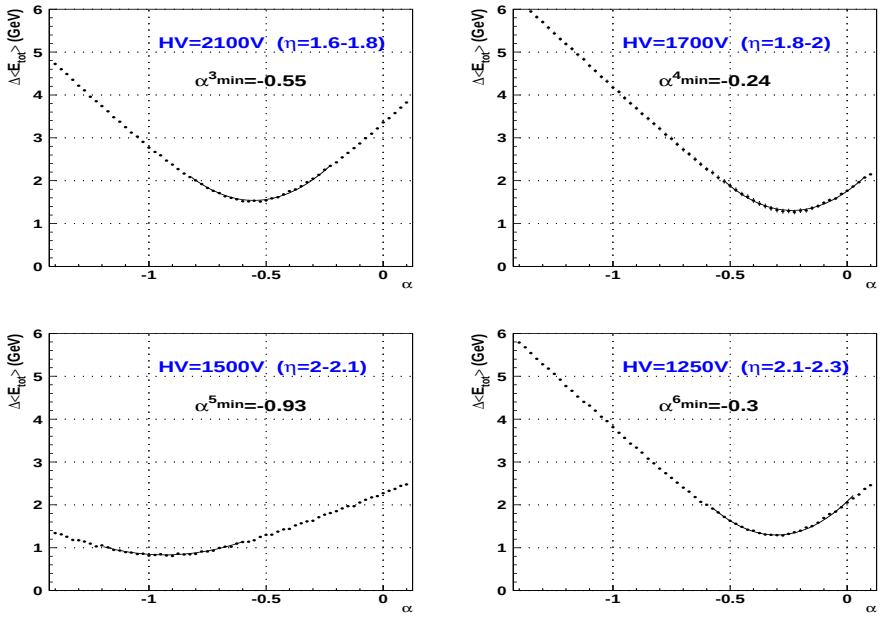

Figure 9: *Variation of total energy dispersion for the 4 HV zones for different α parameters. These results are obtained for optimal filtering. The curve is a parabola fit.*

considered as a lower limit since no clustering effect is present in this case.

The results per sampling are shown in Figure 8b-d. Two expected effects can explain the observed variation of energy deposit:

- Sampling depth (in X_0): for a 100 GeV energy beam, we are mainly sensitive to the step at $\eta = 1.9$ in S1.
- High voltage: in this case, we can distinguish between: *i*) the variation of electric field per sector and *ii*) the relative values of high voltage.

The step at $\eta = 1.9$ for the strips is clearly seen. Effects of high voltage can also be observed in S1 and S2. Because of too small fraction of energy deposit in S3, we do not observe these effects. In Figure 8c, a pattern with a periodicity of four S2 cells (corresponding to one summing board) is observed for both signal processing methods and can not be explained by high voltage effects. This means that other sources of non-uniformity are present. They will be discussed later in this section.

High voltage correction

As already mentioned in section 5.1.2, a weight (w_i^l) is applied on each cell depending on η, the sampling (Si) and the HV sector (l). The energy per sampling (E_{Si}) is thus the

η range	Simulation		Parabola		OF	
	α	β	α	β	α	β
[1.6,1.8]	-0.29	1	-0.55±0.01	0.98	-0.55±0.01	0.99
[1.8,2.0]	-0.31	1	-0.31±0.02	0.99	-0.23±0.02	1.00
[2.0,2.1]	-0.32	1	-0.78±0.02	0.97	-0.93±0.01	0.98
[2.1,2.3]	-0.33	1	-0.22±0.02	1.03	-0.30±0.02	1.02

Table 3: *α and β coefficients in the 4 HV sectors scanned, for the simulation, parabola and OF methods. Errors indicates the variation between the output of first and second iterations.*

weighted sum of the energy in each cell ($E_i(\eta_j, \phi_k)$):

$$E_{Si} = \sum_{j=1}^{N_j} \sum_{k=1}^{N_k} \beta^l \times w_i^l(\eta_j) \times E_i(\eta_j, \phi_k) \tag{12}$$

where β^l is a global factor which takes into account effects due to high voltage setting in the sector l, and $N_j \times N_k$ the number of cells in a $\Delta\eta \times \Delta\phi$ cluster. According to the simulation, these weights can be written:

$$w_i^l(\eta_j) = 1 + \alpha_i^l \cdot (\eta_j - \eta_{center}^l) + O(\eta_j - \eta_{center}^l)^2 \tag{13}$$

η_{center}^l being the center of the considered high voltage sector. Note that, in the case of the simulation,

$$\alpha_i^l = -h_i^l \tag{14}$$

where h_i^l is the expected slope of the energy with respect to η, in each HV sector (Figure 1).

Although other sources of non uniformity affect differently each sampling, cf. Figure 8b-d, we make the following hypothesis (also predicted by the simulation):

$$\alpha^l = \alpha_1^l = \alpha_2^l = \alpha_3^l \tag{15}$$

and β^l parameters are estimated using:

$$\beta^l = \frac{E_{beam}}{E_{tot}^l} \tag{16}$$

where E_{tot}^l is the mean value of total energy per HV sector l, and E_{beam} is the beam energy (100 GeV, here).

α^l parameters are the ones which minimize the total energy dispersion for each high voltage sectors. As input for the first iteration, we choose the α^l coefficients issued from the simulation. Figure 9 shows energy dispersions computed for various α values in the 4 HV sectors. The minimum is obtained by fitting the points with a parabola. A second

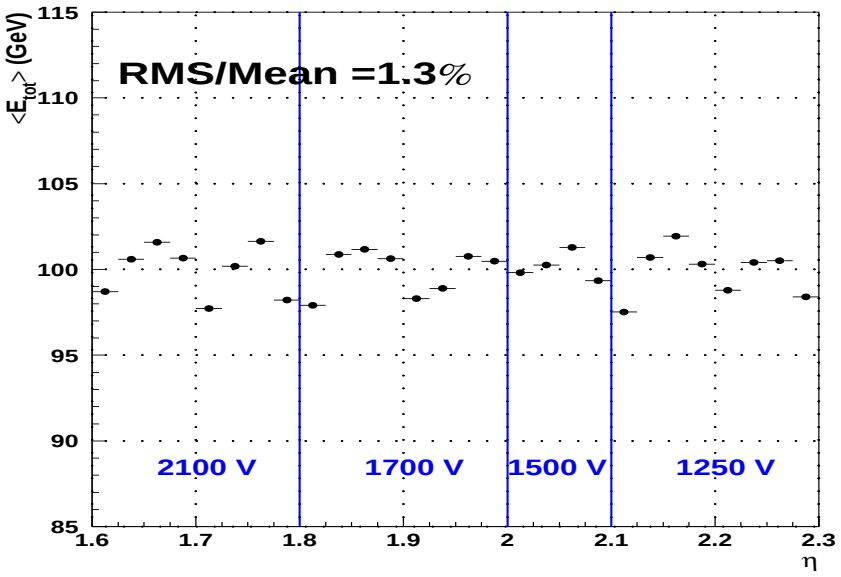

Figure 10: *Total energy after HV correction for optimal filtering versus η.*

iteration is then performed with the new α^l parameters as input. Output α^l values are comparable with input ones within few %.

Table 3 gives parameters obtained for the simulation and the 2 signal processing methods. Errors indicates the variation between the output of first and second iterations. Systematics introduced by the signal processing can be obtained when comparing the results from parabola and OF methods. For α parameters, discrepancies with the simulation may come from other sources of non-uniformity (described below). β coefficients computed with test beam data are not equal to 1, and so HV settings (computed by the simulation) have to be readjusted to obtain a constant mean response of the detector over η[11].

Figure 10 shows the mean total energy as a function of η after high voltage correction, for optimal filtering method. The uniformity is improved by a factor 2 compared to Figure 8a, leading to a total dispersion of 1.3%. The pattern with a periodicity of 4 S2 cells is still observed.

In the following, computed α and β parameters are applied.

Other sources of non uniformity

Two reasons may explain the pattern observed each 4 S2 cells:

- Unsufficient grounding: each electrode connector (on the back side) covers 4 S2 cells

[11] The effect due to the presence of a presampler, not used in this analysis, in the region $\eta = [1.6, 1.8]$ is not estimated.

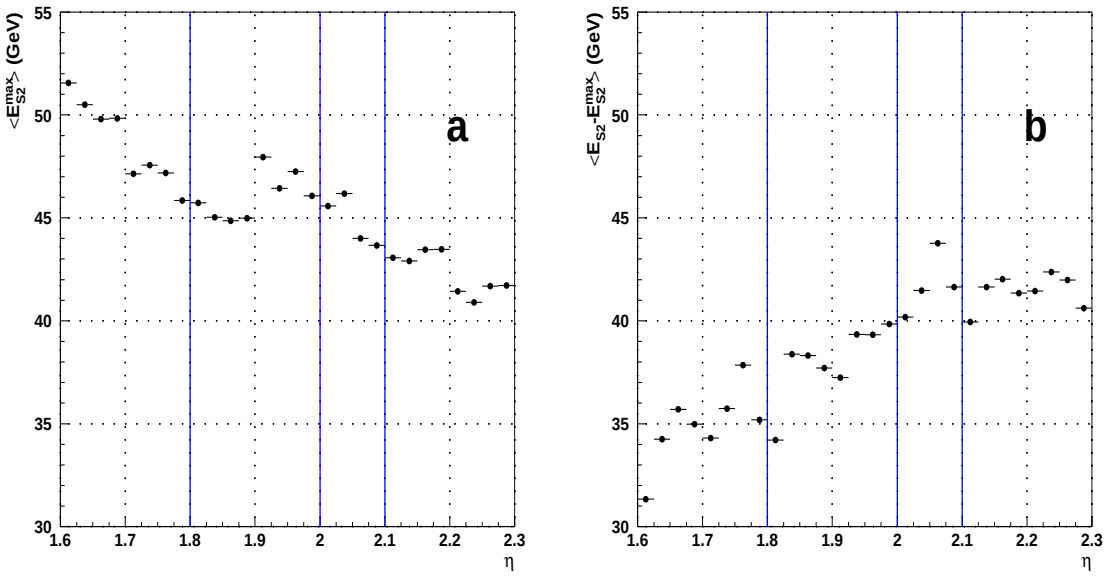

Figure 11: *a) Central and b) other cluster cell energies in S2, as a function of η.*

and ground is present only at low η side of the connector. This asymmetry in the grounding modify the electronic parameters (mainly inductances), thus the signal shape and amplitude. Solution, to correct for this effect, is discussed in detail in section 6.2.

- Crosstalk in cold electronics: it is coming from back mother and summing boards, depends on η, and is of the order of few percents. The insufficient grounding, mentioned above, also contributes to the crosstalk. As it is proportional to the energy, it affects mainly cells surrounding the one with maximum energy deposit. Figure 11 shows the energy in S2 of: a) the central cell and b) other cells in the cluster ($E_{S2}^{oth} = E_{S2} - E_{S2}^{max}$), respectively. As expected, E_{S2}^{max} decreases smoothly in regions $\eta = [1.6, 1.9]$ and $[1.9, 2.3]$ because of the S2 cell size. In contrary, E_{S2}^{oth} increases with η and the same pattern as in the Figure 10, with similar amplitudes, is observed. This drives us to consider the crosstalk in cold electronics as a possible source of non uniformity. Solutions to correct for this effect are discussed in section 6.3.

5.2.2 Detailed structure of the η scan

Figure 12a shows the total energy as a function of the barycenter computed in S1. Local parabolic shapes inside each S2 cell reflects the η lateral leakage out of the cluster. Figures 12b-d show the energy for strip, middle and back samplings. In S1, the energy is slightly increasing in [1.7,1.8], [1.9,2.0] and [2.1,2.2] ranges. These effects may come from the HV correction done globally and not per sampling. As most of the energy is deposited in S2,

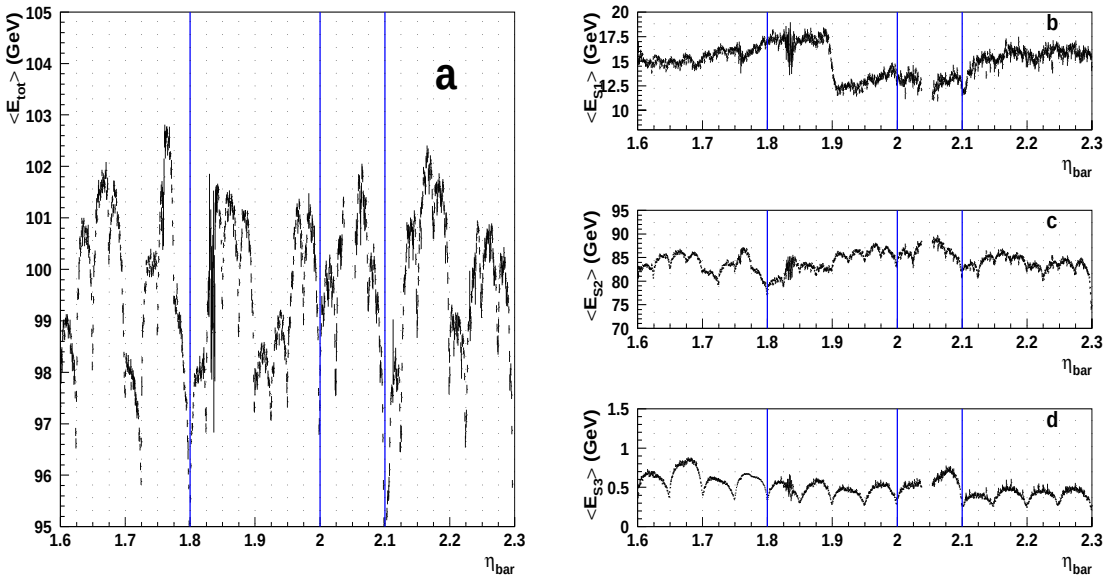

Figure 12: *a) Total and b-d) sampling energies versus η. A cluster matching 5×5 in S2 is chosen.*

structure of η lateral leakage is the same as E_{tot}. In S3, the periodicity of the pattern is double and reflects the η cell size. The effect of lateral leakage is much more pronounced because only one cell is used in this sampling.

The variation of the total energy with respect to η barycenter is parametrized with the function:

$$F_1(\eta_{bar}) = C_0 \cdot f_1(\eta_{bar}) = C_0 \cdot \left(1 + C_1 \cdot \left[(\eta_{bar} - \eta_{S2}^{center}) - C_2\right]^2\right) \tag{17}$$

where C_0 is the maximum of the parabola, C_1 its curvature (sensitive to the cluster size) and C_2 the position of the maximum with respect to the center of the S2 cell (η_{S2}^{center}). As an example, Figure 13a shows the total energy as a function of η barycenter at $\eta = 1.94$. After correction, a residual pattern with the periodicity of strip cell size is still visible (effect of $\sim 0.2\%$) and can be explained by 'S-shapes' of each strips. This is confirmed by the simulation.

Parabola curvature (C_1) and position of the maximum (C_2) as a function of η are plotted in Figure 14, as well as their distributions. C_1 is about -0.1 and is rather constant with η which may indicate no clustering effect using a 5×5 cluster. C_2 varies around 0 with a dispersion of 14% because the parabolic shape is distorted by the remaining cell by cell energy variation.

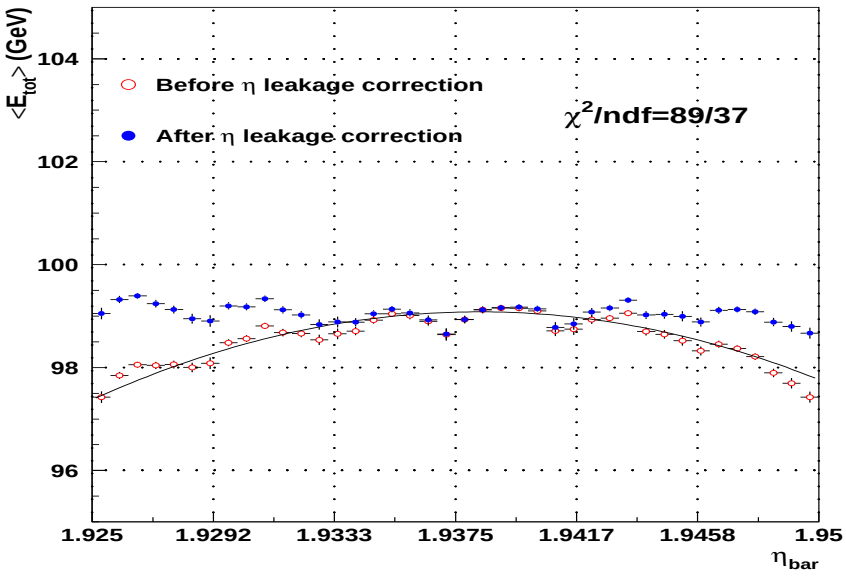

Figure 13: *Total energy versus η before and after the η leakage corrections (η = 1.94). Vertical dotted lines represent strip cells. The curve is a parabola.*

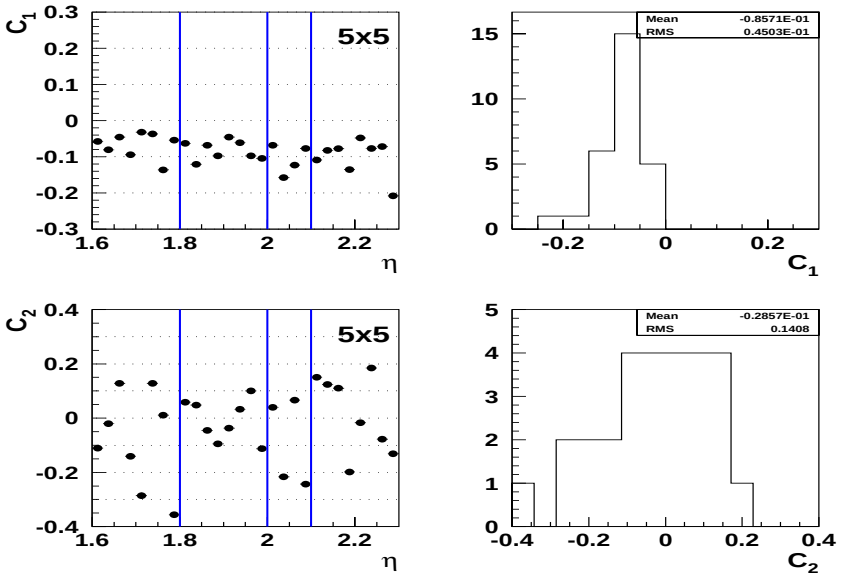

Figure 14: *Fitted parameters of η leakage correction versus η and their distributions.*

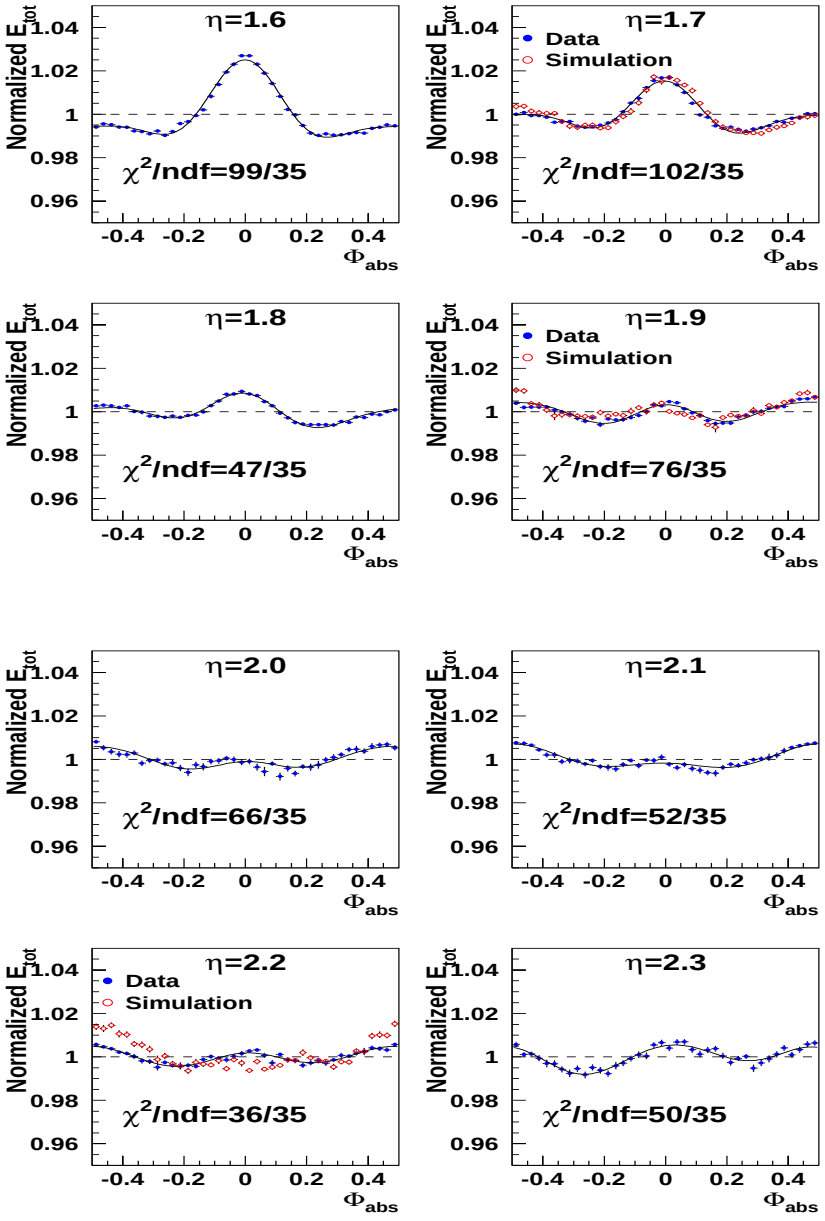

Figure 15: *ϕ-modulation in absorber unit for 8 η values for the test beam data (full circle) and 3 η values, η=1.7, 1.9, 2.2 for the simulation with charge collection (open circle). A 5×5 cluster is used in S2. The curve is the function (Fourier series) used to correct for these ϕ-modulation.*

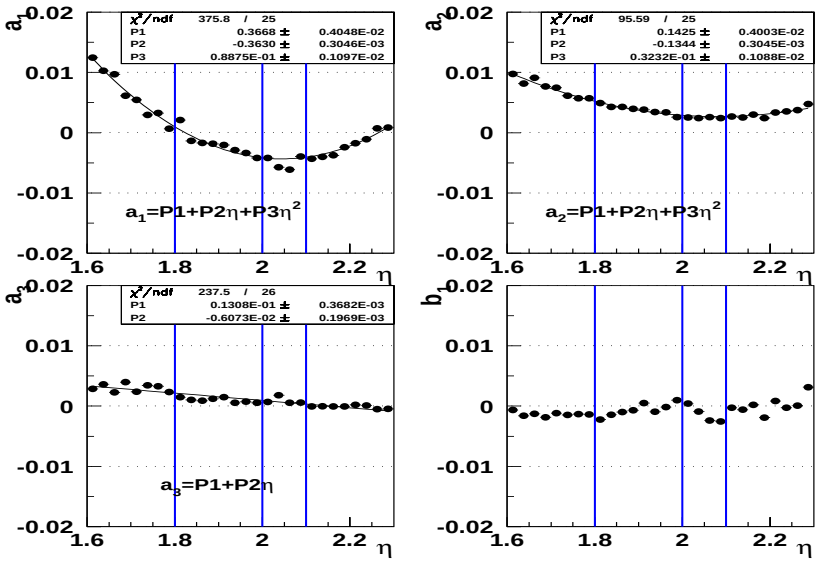

Figure 16: *Fitted parameters of ϕ-modulation versus η. a_1 and a_2 are fitted with a parabola and a_3 with a slope.*

5.2.3 ϕ-modulation

The accordion geometry has a direct impact on the uniformity of the detector response with respect to ϕ. Figure 15 shows the ϕ modulation in absorber unit (ϕ_{abs}) for different η values. Test beam data and simulation with charge collection, for 3 η values, are in good agreement for amplitude and shape of the ϕ modulation, except for $\eta > 2.1$.

Dependence of the total energy as a function of the ϕ barycenter computed in S2 (ϕ_{abs}) is usually parametrized with Fourier series:

$$F_2(\phi_{abs}) = a_0 \cdot f_2(\phi_{abs}) = a_0 \cdot \left(1 + \sum_{i=1}^{3} a_i \cdot \cos(2\pi i \phi_{abs}) + b_1 \cdot \sin(2\pi \phi_{abs})\right) \quad (18)$$

where a_0 is the mean total energy, a_i are the even coefficients. b_1 is an odd coefficient which takes into account calorimeter local defects.

Fitted parameters of ϕ-modulation versus η are shown in Figure 16. Their dependence with η reflects the geometry (folding angle, gap) variation. Cosine parameters (a_i) vary smoothly and can be fitted with a parabola for a_1 and a_2 and a straight line for a_3. The sine parameter (b_1) is small in amplitude compared to a_1 and a_2 showing that calorimeter defects are well under control (for $\phi_{cell} = 10$).

5.2.4 Energy resolution

Figure 17 shows the total energy distribution after all corrections are applied. An improvement of energy resolution by 12% ($\sigma_E/E = 1.03\%$ instead of 1.15%) is obtained.

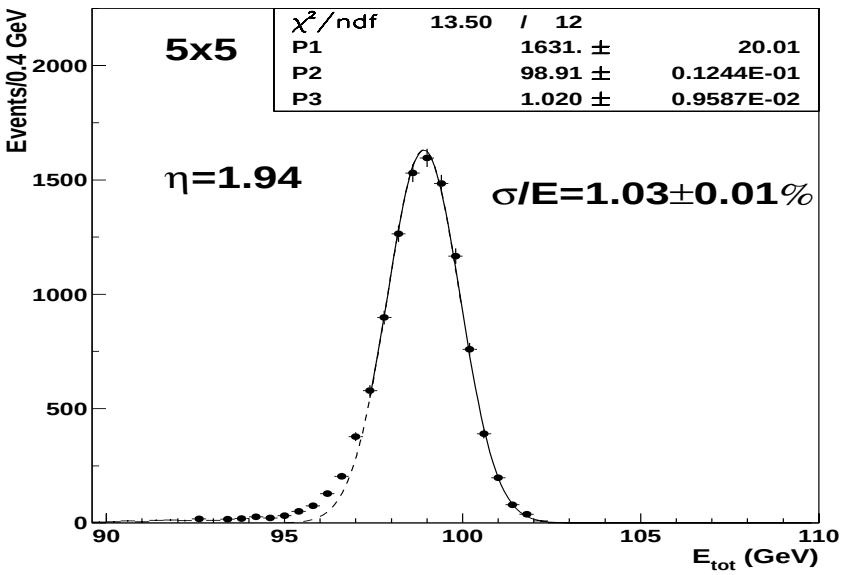

Figure 17: *Total energy distribution at $\eta = 1.94$ for a 5×5 cluster in S2. All corrections are applied, but the beam spread is not subtracted.*

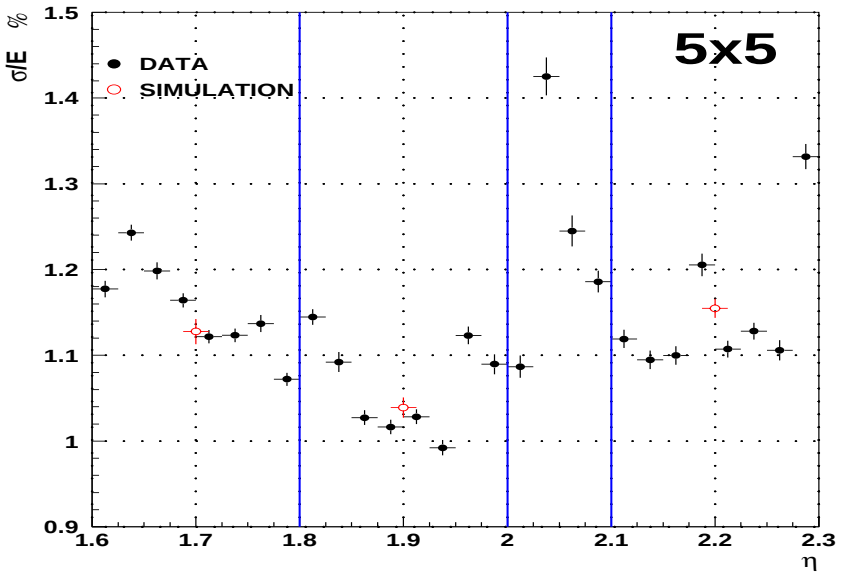

Figure 18: *Energy resolution versus η, after the beam spread is subtracted. A cluster matching 5×5 in S2 is chosen.*

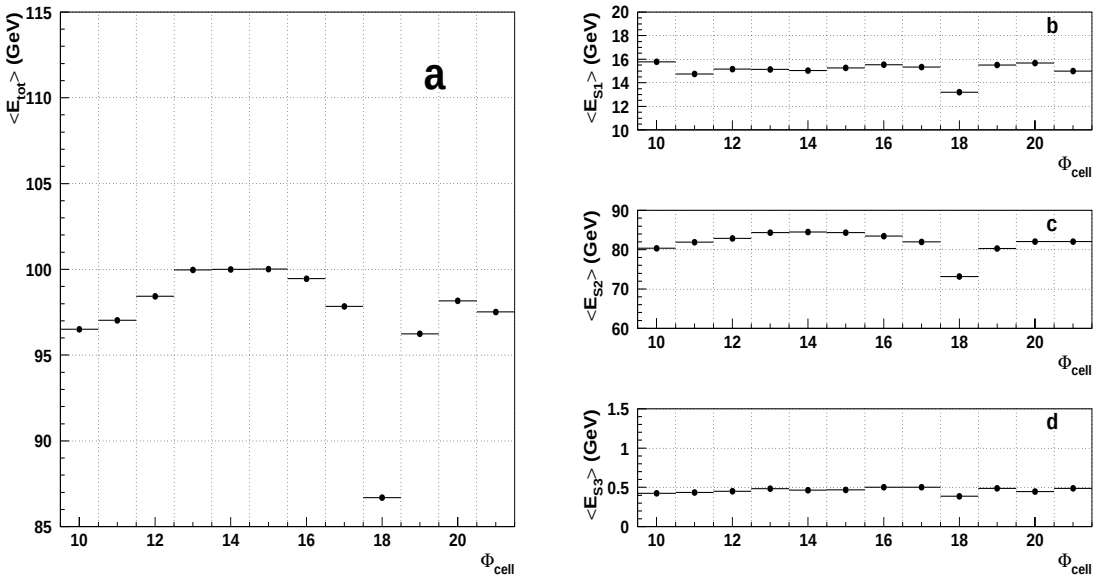

Figure 19: *a) Total and b-d) sampling energies as a function of ϕ_{cell}. A cluster matching 3×5 in S2 is chosen.*

Figure 18 shows the energy resolution as a function of η for test beam data, after the beam spread is subtracted, and simulation (in 3 points). Except for a cell at $\eta = 2.025$ (dead cell region of the strip) and 2.28 (dead HV zone for $\eta = [2.3, 2.5]$), all values are below 1.25% and coincide with the simulation. The energy resolution has its minimum around $\eta = 1.9$. It corresponds to the region where the sampling fraction is still high (around 22%) and the phi-modulation amplitudes already low (less than 1%).

5.3 ϕ scan

ϕ scans were only performed in the η region [2.15,2.25], centered on a high voltage sector (1250 V), because of HV problems. To obtain a complete ϕ coverage, runs are taken each half ϕ S2 cell ($\Delta\phi = 0.0125$).

The S2 ϕ cell size decreases, versus η, from 5.2 to 1.8 cm ($\sim$ 2.5 cm at $\eta = 2.2$). Taking into account the beam size in ϕ, a complete coverage can be obtained with only 2 runs per S2 cell at $\eta = 2.2$.

Some singular channels were unfortunately present in this region. This lead us to consider only one ϕ scan at $\eta = 2.1625$[12], as reference for ϕ uniformity study, and a 3×5 cluster size in S2. This has a direct implication on the results presented in this section: *i*) γ coefficient applied in section 5 was re-computed, *ii*) corrections in η differ from the ones calculated for the η scan, and *iii*) the energy resolution is degraded.

[12]This represents 23 runs with 30000 events each.

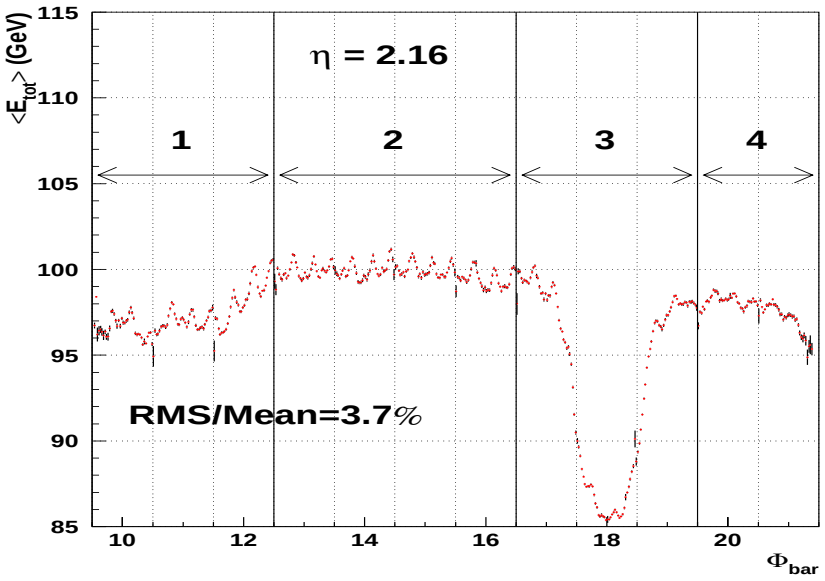

Figure 20: *Total energy as a function of ϕ barycenter computed in S2 at η=2.16. Dotted vertical lines represent separation between cells, and solid lines zones of interest.*

5.3.1 Global view of the ϕ scan

At this step of the analysis, no corrections are applied yet, except the HV ones computed in section 5.2.1. We consider only events where the cell at $\eta = 2.1625$ is the one with maximum energy deposit.

Figure 19a shows the total energy as a function of middle cell number. The γ value is computed for ϕ_{cell} = 13-16. All E_{tot} values are in the range 96-100 GeV, except for $\phi_{cell} = 18$, which its central electrode was not supplied with high voltage (HV1 side)[13]. This also affects cells $\phi_{cell} = 17$ and $\phi_{cell} = 19$, which include $\phi_{cell} = 18$ in their clusters.

The energy per sampling is shown in Figures 19b-d. In S1 and S3, the energy has no ϕ dependence. In S2, the variation is of the order of 6% and similar to the one observed in Figure 19a.

5.3.2 Detailed structure of the ϕ scan

A more detailed view of the calorimeter response can be obtained when looking at the total energy versus the ϕ barycenter computed in S2 (ϕ_{bar}), cf. Figure 20. The overall dispersion normalized to the mean energy is about 4% and a periodicity in the ϕ-modulation is observed. Figure 20 can be divided in four different zones:

1. ϕ_{cell} = 10-12: increasing of mean energy.
2. ϕ_{cell} = 13-16: constant value of mean energy (plateau).

[13] A short circuit in the gap was detected after the complete stacking of the module.

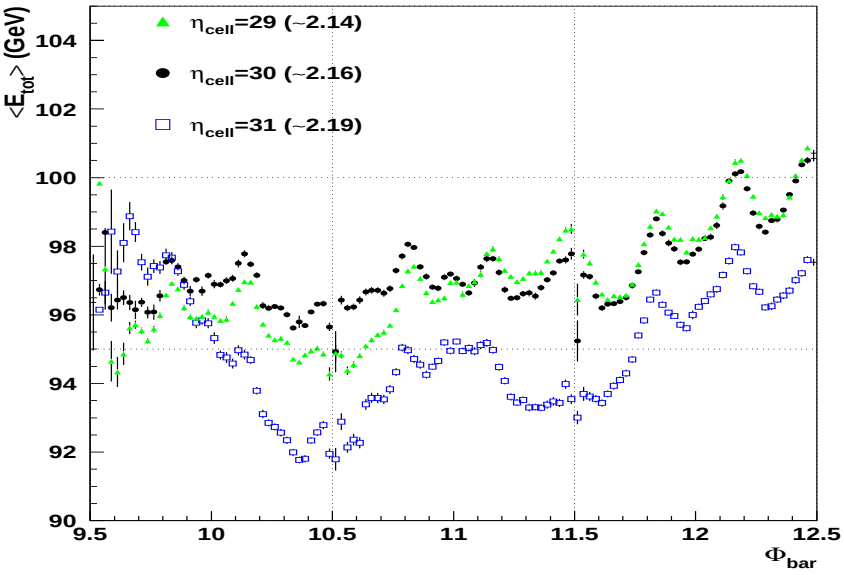

Figure 21: *Total energy as a function of ϕ barycenter for 3 consecutive η cells in the zone 1 ($\phi_{cell} = 10 - 12$).*

3. ϕ_{cell} = 17-19: region concerned by the effect of dead HV1.

4. ϕ_{cell} = 20-21: low decreasing of mean energy.

Zones 1, 3 and 4 are studied in detail in this section. Zone 2 is our reference for ϕ uniformity study, and is treated in section 5.3.3.

Zone 1

A zoom on this zone is shown in Figure 21. The ϕ-modulation (in the same ϕ region) for other cells is superimposed. Distorted ϕ-modulations for ϕ_{cell} = 10-11 are observed for all considered cells with the same amplitude. In contrary, ϕ-modulation for ϕ_{cell} = 12 are not distorted but stretched to reach the plateau region.

A possible explanation for these effects can be found in the stacking process. Starting from ϕ_{cell} = 12, a stress was applied on the absorbers to control the sagging, cf. section 2.2.1. This introduces an uncertainty on the detector response for cells 10-11 (6 absorbers), and may lead to the distortion of ϕ-modulation in this region. Furthermore, no sagging evolution was seen for ϕ_{cell} = 12-14 and a transition is expected in cell ϕ=12, which may be the sudden increase of total energy for this cell.

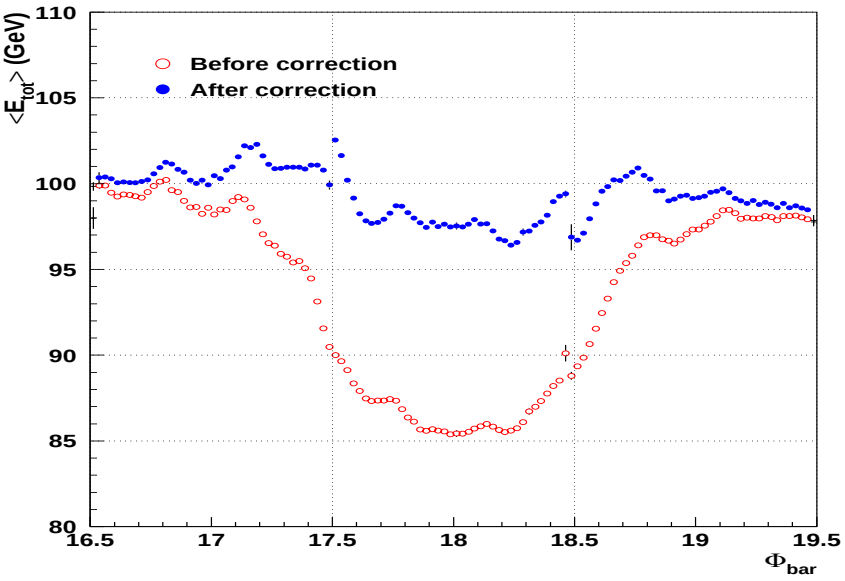

Figure 22: *Total energy as a function of ϕ barycenter in zone 3 before and after dead electrode correction.*

Zone 3

As already said in section 5.3.1, high voltage is not supplied for HV1 side of the central electrode of $\phi_{cell} = 18$. This results in an unefficiency of $1 - \frac{1}{6} \sim 0.83$, and consequently the cell is weighted by a factor 1/0.83 (this correction is applied in the rest of the analysis).

Figure 22 shows the total energy before and after this correction is applied. It allows to reduce the energy dispersion by a factor of about 2.5. However, this correction systematically underestimate the energy in $\phi_{cell} = 18$ and overestimate the neighbor cells.

A more refined way of correcting this effect can be, for example, to apply weights depending on ϕ barycenter. We did not consider this option because this implies a dedicated study out of the scope of this note.

Zone 4

A low decrease of energy is observed in this zone (ϕ_{cell} = 20-21). It might be a consequence of the stacking, sagitta value reaching 2 mm in this region.

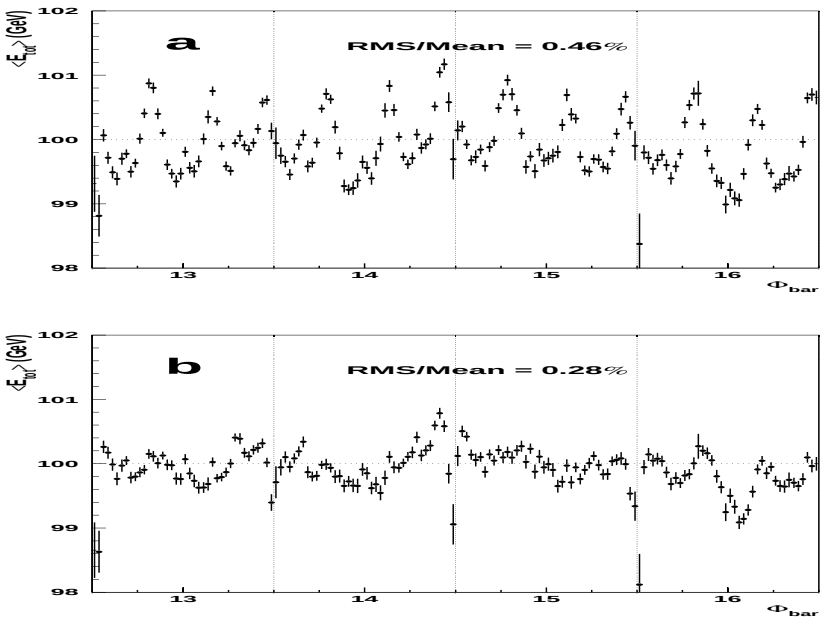

Figure 23: *Total energy as a function of ϕ barycenter in zone 2: a) before and b) after ϕ modulation correction. RMS/Mean computation takes into account the errors on each points.*

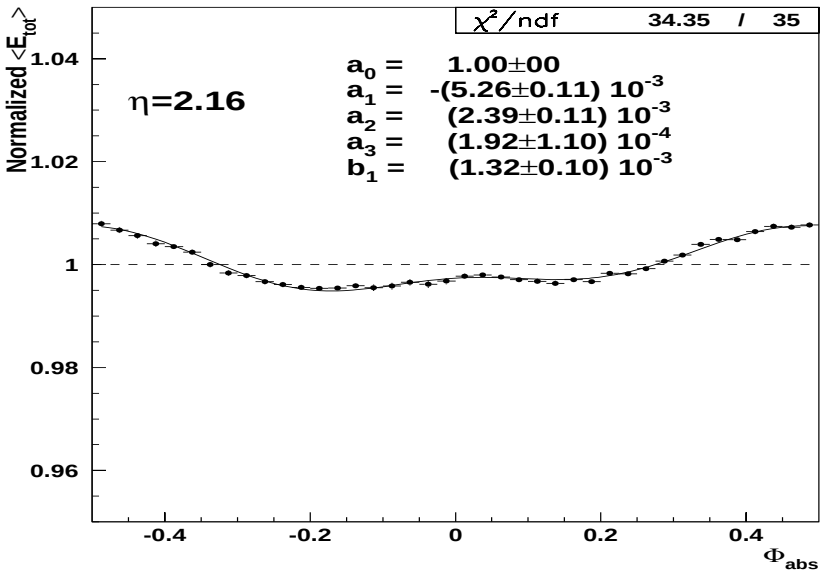

Figure 24: *Average ϕ-modulation computed on 4 cells at $\eta = 2.16$.*

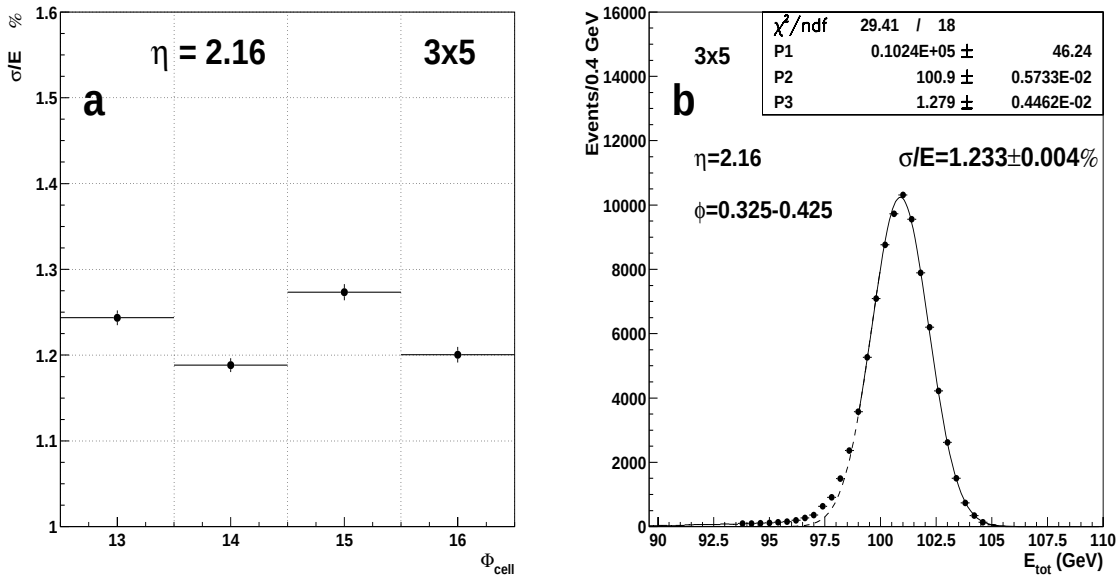

Figure 25: *a) Energy resolution versus ϕ at $\eta = 2.16$. b) Total energy distribution for ϕ_{cell} = 13-16 after all corrections are applied. In both case, a cluster matching 3×5 in S2 is chosen, the beam spread is subtracted and all corrections are applied.*

5.3.3 ϕ uniformity estimate and energy resolution

Even if only 4 ϕ cells are concerned, a first estimate of ϕ uniformity can be obtained when studying zone 2, where no major stacking problems occured. A RMS of 0.6% and 0.2-0.3% is expected from simulation, before and after correction for ϕ-modulation, respectively [15].

Figure 23a shows the total energy as a function of ϕ in the region ϕ_{cell} = 13-16. The measured energy dispersion is about 0.5%. To correct for ϕ-modulation, an average over the 12 absorber plates is performed. The averaged normalized modulation in absorber unit, is shown in Figure 24. The parameters extracted from the fit are slightly different from the ones presented in Figure 16 because reflecting the sagging variation during the stacking. Figure 23b shows the total energy after this correction was applied. The resulting energy dispersion is now about 0.3%, in correct agreement with the simulation.

The final energy resolution, after correcting for the η lateral leakage and subtracting the beam spread, is shown in Figure 25a. Energy resolution is constant over ϕ at 1.2-1.3%. Higher values compared to the results presented in Figure 18a, are mainly due to the cluster choice. Figure 25b shows the total energy distribution for ϕ_{cell} = 13-16 after all corrections are applied. Subtracting the expected (using the simulation) 1% contribution from the sampling term and the noise term (0.2%), we obtain 0.7% for the constant term over 4 cells.

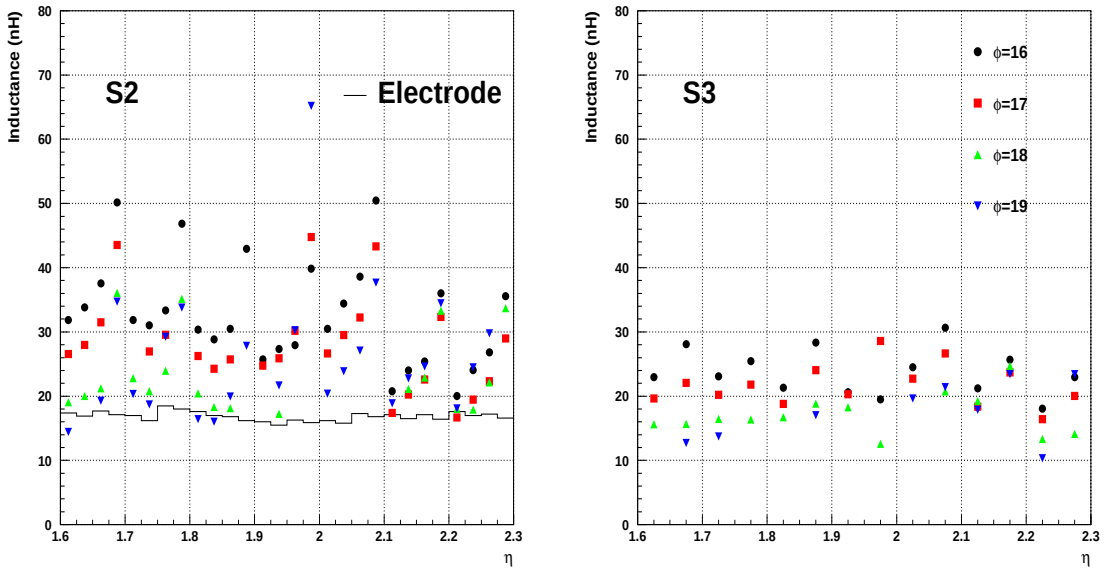

Figure 26: *Measured inductances on S2 and S3 for the module 0 with an RLC meter, after taking out the mother boards. The full histogram shows the theoretical electrode inductance [16].*

6 Solutions to improve non uniformities

Since the data taking in 1999, several solutions were proposed and tested to correct for the main sources of non uniformity.

6.1 Improvement of the stacking procedure

The stacking procedure is now improved concerning: *i*) the cleanliness of the stacking room and of all detector components (electrodes, honeycomb spacers and absorbers), *ii*) the thickness and the fabrication of honeycomb spacers. One third of a module was stacked in these conditions and none HV problem was detected at warm. In addition sagitta (sensible to point *i*)) was kept around 0 $\pm$0.5 mm.

6.2 Reduction of the inductance variation

Inductance (effective and real) variation across the module significantly distorts the signal shapes (in a different way for calibration and physics). It is thus mandatory to reduce as much as possible their variation across the module by: *i*) rendering uniform the different strip lengths in the cold electronics boards and *ii*) improving the grounding.

Inductance measurements with an RLC-meter were performed on the back side of the module 0. As mother boards were previously unplugged, the signal was sent through

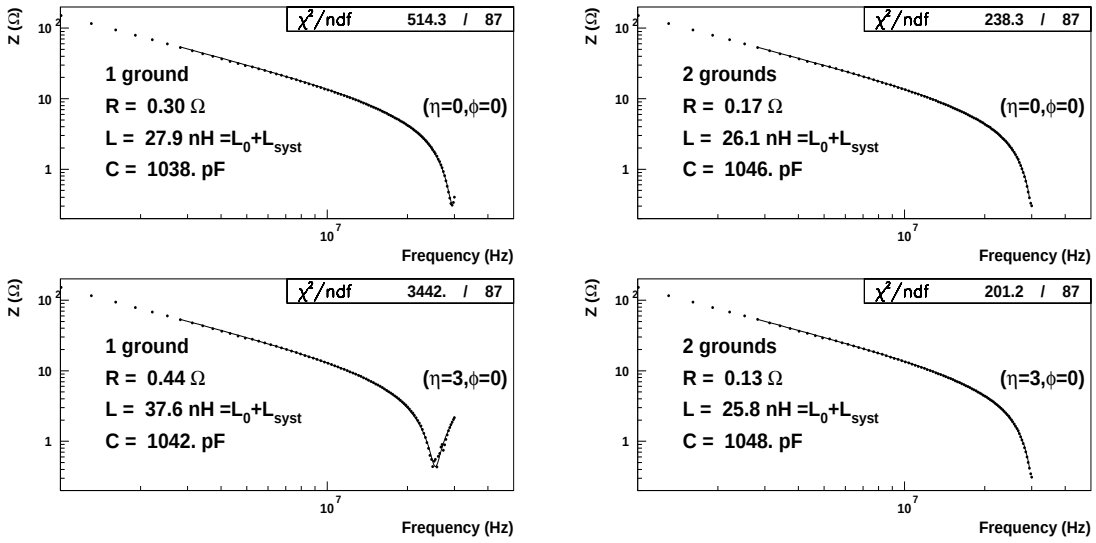

Figure 27: *R, L and C extracted for two channels located on each side of the summing board, with one ground (left plots) and two grounds (right plots). An extra inductance (L_{syst}) was added to reach the resonance before 30 MHz. The results are obtained for one ϕ line ($\phi = 0$).*

the summing boards. Measured inductances are shown in Figure 26 and two general effects are observed:

1. A variation of inductance versus ϕ: it comes from the variation of the summing board strip line lengths. This length depends on the distance to the mother board connection and, thus increases with ϕ. To cure this problem, we chose the maximum value of the strip length as reference for all the other strips. In such a way, all strips of a summing board have an equal length. This was already done for η region [2.1,2.2] and was extended to all summing boards in the final design.

2. A variation of inductance versus η: it was traced back to an unsufficient (asymmetric) grounding. To confirm this assumption, RLC -meter measurements were performed on summing boards alone, loaded with a toy calorimeter (precisely measured capacitances, C = 1.04 ± 0.01 nF, were soldered on the back of the summing board). The effective inductances (L_0), extracted from the fit[14] are shown in Figure 27 for two channels located at each side of the summing board, labelled $\eta = 0$ and $\eta = 3$ (both on the same ϕ line, $\phi = 0$). To reach the resonance before 30 MHz, an extra inductance (L_{syst}) was added. When only one ground exists, the measured inductance is higher by 10 nH for the channel located far from the ground

[14] $Z = \sqrt{(R^2 + [1/(2\pi Cf) - 2\pi fL]^2)}$, where Z is the measured impedance (Ω) and f is the input frequency.

	$\eta = 0$	$\eta = 1$	$\eta = 2$	$\eta = 3$
1 ground	27.9	28.9	30.5	37.6
2 grounds	26.1	27.7	27.7	25.8

Table 4: *Inductance values (L_0+L_{syst} in nH) for S2 channels for one ϕ line. L_{syst} is an extra inductance added to reach the resonance before 30 MHz.*

($\eta = 3$), while equal values are obtained when two grounds are implemented. Complete results with two grounds are shown in Table 4. Because similar problems were encountered in the barrel, it was decided to add an additional ground connection on each electrode connector, in the back side. Consequently summing and mother boards were also modified in accordance.

It's worth noticing that using these inductance measurements, it is possible to partly correct the non uniformities seen in Figure 10 [17].

6.3 Reduction of inductive crosstalk in mother boards

Other modifications were applied to mother boards in order to reduce their contribution to the crosstalk in S2 and S3. Redesigned mother boards were tested and crosstalk amplitude was reduced by a factor 2 to 4 [6].

7 Conclusions

Uniformity scans were performed over the half equipped outer wheel of the EMEC module 0 with a 100 GeV positron beam. The results were shown for: *i*) one ϕ line in the η range [1.6,2.3] (4 HV sectors out of 7), and *ii*) several η lines in the region around η=2.2 (ϕ_{cell} = 10-21). Results were obtained using the last version of the optimal filtering for the calibration, as well as for the physics data.

Main conclusions can be summarized as follow for the η scan (5×5 cluster in S2):

1. A method was set up to correct for the high voltage effects. However results suffer from other sources of non uniformity and it was not possible to obtain definitive settings for the HV. Therefore, for the next module in test beam, we will use the ones predicted by the simulation.

2. The calorimeter response dispersion after HV correction is around 1.3%. No attempts were made to correct for the variation of inductance in η and ϕ.

3. ϕ-modulation variations along the scan can be fitted by a 4-parameter Fourier serie. These coefficients vary smoothly and can be parametrized as a function of η. A good agreement is found between test beam data and simulation.

4. The energy resolution obtained is everywhere better than 1.25 % at 100 GeV with a minimum of 1% around $\eta = 1.9$, as expected by the simulation.

Concerning the ϕ scans (for a 3×5 cluster in S2), we can conclude that for a detector stacked in optimum conditions (no sagging and no HV problems), the calorimeter response dispersion, after all corrections are applied, can be kept around 0.3%. This is in agreement with the simulation, and a constant term of about 0.7% can be extracted in this region, covering 4 S2 cells.

Main sources of non uniformities during stacking are the sagging of the detector and the presence of gaps which do not hold the nominal HV values. Progress were made since 1999 and both problems are now under control. On the electronics side, an unsufficient grounding was brought to light, resulting in a variation versus η of the effective inductance, with a periodicity of one summing board. This may have a direct impact on the calorimeter response dispersion in η. A solution was proposed and test bench results are encouraging. A definite confirmation will be obtained with the 2001 test beams. Less crosstalk in the mother boards as well as equalized inductances for the summing boards are also improvements already on hand. With all these modifications, the constant term may also be improved.

Acknowledgements

We want to thank Christophe de La Taille, Dominique Sauvage and Laurent Serin for their constant help and support for RLC and summing boards test bench measurements.

Special thanks to Chafik Benchouk, Emmanuel Monnier and Sylvain Tisserant for carefully reading this manuscript.

References

[1] ATLAS Collaboration, *ATLAS Liquid Argon Calorimeter Technical Design Report*, CERN/LHCC/96-41.

[2] ATLAS Collaboration, *ATLAS Calorimeter Performance*, CERN/LHCC/96-40.

[3] P. Barrillon et al., *Uniformity Scan in the Crack and the Inner Wheel of the Electromagnetic Endcap Calorimeter*, Note in preparation.

[4] O. Martin, E. Monnier and S. Tisserant, *Update of some Geometrical Parameters for the ATLAS E.M. End-Cap Calorimeter*, ATLAS-LARG-96-047.

[5] J. Colas et al., *Crosstalk in the ATLAS Electromagnetic Calorimeter*, ATL-LARG-2000-004

[6] P. Pralavorio and D. Sauvage, *Review of the crosstalk in the module 0 of the Electromagnetic Endcap Calorimeter*, ATL-LARG-2001-006.

[7] K. Elsener, *Short Introduction to the use of the H6 beam*,
http://sl.web.cern.ch/SL/eagroup/beams.html#h6

[8] J. Spanggaard, *Delay Wire Chambers. A Users Guide*, SL-Note-98-023 *BI*

[9] A. Mirea, PhD Thesis, *Optimisation d'un calorimètre bouchon pour l'expérience ATLAS et étude des modèles SUGRA avec violation de la R-parité (Couplage à 3 leptons) avec le détecteur ATLAS*, CPPM-T-1999-02.

[10] D. Nicod, D. Zerwas and R. Zitoun, *EMTB User Guide*,
http://atlasinfo.cern.ch/Atlas/GROUPS/LIQARGON/TESTBEAM/emtbdoc.ps

[11] W.E. Cleland and E.G. Stern, *Signal processing considerations for liquid ionization calorimeters in a high rate environment*, NIM A338(1994) 467-497.

[12] P. Barrillon et al., *Optimal Filtering in the Electromagnetic Endcap Calorimeter*. Note in preparation.

[13] B. Mansoulie and J. Schwindling, *Using Multi Layer Perceptrons in PAW*,
http://schwind.home.cern.ch/schwind/MLPfit.html

[14] J. Colas et al., *The LARG Calorimeter Calibration Board*, ATL-LARG-2000-006.

[15] ATLAS Collaboration, *Detector and Physics performance Technical Design Report*, CERN/LHCC/99-14, p.112-113.

[16] F. Djama, L. Hervas and C.P. Marin, *Copper-Polyimide Multi-Layer Electrodes for the End-Cap Electromagnetic Calorimeter*, ATL-LARG-98-088.

[17] L. Neukermans, P. Perrodo and R. Zitoun, *Understanding the ATLAS electromagnetic barrel pulse shapes and the absolute electronic calibration*. Note in preparation.

Appendix 1: Correction of singular channels

1. $\eta_{cell} = 179$, $\phi_{cell} = 2$ in S1

A drop of energy of about 1/3 was observed for this strip, along the η scan. It was traced back to a broken resistor, in a HV side (HV2), on the 9th electrode. This was confirmed by the fact that no such effect was seen for the calibration. Correction consists in applying a factor 1.33 on this cell energy when S2 barycenter in ϕ is located in front of the faulty strip.

2. A S2-S3 short-circuit ($\eta = 1.65$, $\phi_{cell} = 10$)

We apply the following procedure to estimate the correct energy deposit in both cells. Because of the short circuit, the output signal is equally shared between the 2 cells and so:

$$A_2^m = A_2^t - \frac{1}{2}A_2^t + \frac{1}{2}A_3^t = A_3^m \tag{19}$$

where A_i^m (A_i^t) is the measured (true) output signal maximum amplitude (in ADC counts). Introducing

$$\alpha = \frac{A_2^t}{A_3^t} \tag{20}$$

we can then parameterize the true amplitude in S2 as:

$$A_2^t = \frac{2\alpha}{\alpha+1}A_2^m \ , \quad A_3^t = \frac{A_2^m}{\alpha} \tag{21}$$

As S3 is covering 2 S2 cells in η (A_2 and A_2'), a more correct parameterization is:

$$A_2^t = \frac{2\alpha}{\alpha+1}A_2^m - \frac{1}{\alpha+1}A_2^{m'} \ , \quad A_3^t = \frac{A_2^m}{\alpha} + \frac{A_2^{m'}}{\alpha} \tag{22}$$

The determination of the α parameter is obtained using the neighboring cells as reference. We then use r_0, r_1 and r_2 coefficients from neighboring cells in ϕ to calibration these 2 cells.